CrossMark

Multi-doped Brookite-Prevalent TiO$_2$ Photocatalyst with Enhanced Activity in the Visible Light

Sebastiano Cataldo[1,2] · Bert M. Weckhuysen[1] · Alberto Pettignano[2] · Bruno Pignataro[2]

Abstract

Enabling solar and/or visible light-driven photocatalysis is a crucial step to access innovative applications in environmental science and sustainable energy. Titanium dioxide is the most used photocatalyst because of its low cost and toxicity, however it is also limitedly active under visible light irradiation due to its wide band gap. Among its polymorphs, brookite holds promising optoelectronic properties for visible light photocatalysis, which have to the best of our knowledge been limitedly exploited. Here, a C,S,N-doped brookite-based TiO$_2$ has been prepared via a rapid one-pot sol–gel synthesis. Besides substantially extending the visible light absorption via band gap narrowing, its photocatalytic activity has been enhanced further by optimising valence and conductive band position and by minimising electron–hole recombination. These materials showed a 100% boost in visible light absorption along with nearly 50-times enhanced photocatalytic activity per specific surface area than standard TiO$_2$ Degussa-P25, giving the best performance among the brookite-based photo-catalytically active materials and resulting among the TiO$_2$ top-performers under visible light.

Graphical Abstract
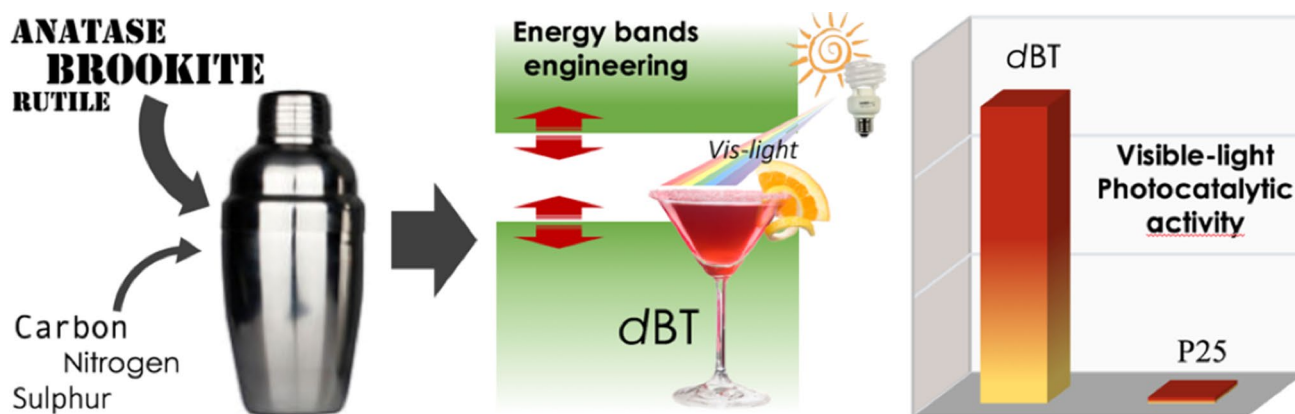
Keywords Brookite · Visible-light photocatalysis · Titanium dioxide · Heterogeneous catalysis · Doping

✉ Sebastiano Cataldo
sebastiano.cataldo@unipa.it

1   Inorganic Chemistry and Catalysis Group, Debye
    Institute for Nanomaterials Science, Utrecht University,
    Universiteitsweg 99, 3584 CG Utrecht, The Netherlands

2   Dipartimento di Fisica e Chimica, Università degli Studi di
    Palermo, Viale delle Scienze Ed.17, 90128 Palermo, Italy

1 Introduction

In the very large spectrum of naturally occurring chemical processes, heterogeneous photocatalysis has drawn ever-growing attention because of the many interesting and innovative applications it can inspire. Air pollutant photodegradation, [1, 2] self-cleaning surfaces, [3, 4] wastewater photodepuration [5, 6] and water-splitting hydrogen

production [7–10] are only few examples where this environmental friendly process is virtuously involved to convert sunlight in chemical energy. The operation mechanism of heterogeneous photocatalysis relies on the optoelectronic properties of semiconductors, particularly metal oxides. These are able to absorb light and generate free electrons and holes that diffusing at the material surface trigger a series of redox processes.

From the time of Honda and Fujishima [7] who first discovered this phenomenon by titanium dioxide (TiO_2), this metal-oxide semiconductor has been the most investigated material for photocatalytic applications [11] because of its high mechanical and chemical stability, low cost and limited toxicity. Regrettably, among the main drawbacks that severely limits the applicability of TiO_2 there is the fast electron–hole recombination that suppresses the quantum efficiency and its wide band gap (up to 3.6 eV) [12] making this photocatalyst active only in presence of ultraviolet light. Contrariwise, by considering self-cleaning or water-splitting applications in ambient condition ideal photocatalysts must be able to largely exploit sunlight, which actually includes 43% of visible radiation (400–700 nm) and only 3% of UV photons (< 400 nm). Also, photocatalysis under visible light would allow taking full advantage of artificial illumination including LED and fluorescent lamp in indoor environments, which mainly emit in this range.

TiO_2 comes in nature essentially in the form of three polymorphs: anatase, rutile and brookite. While the first is the most extensively studied and the second usually showed limited photocatalytic performance, [13, 14] brookite-based materials have received very few attention because of challenging preparation and only recently they are going under the spotlight despite having promising properties [15]. Indeed, though it is a still debated question it seems that brookite has the lowest energy band-gap [12, 16–19] with values ranging between 3.0 and 3.4 eV against about 3.4 and 3.6 eV for rutile and anatase, respectively [12]. In addition, it has been reported that brookite is characterized by an indirect band gap [15, 20–22] yielding longer electron–hole recombination time, since electronic decay needs to couple with lattice phonons. As a consequence, electrons and holes would have more time to reach the catalyst surface and interact with target molecules. Lopez-Munoz et al. [23] prepared pure brookite and mixed anatase-brookite with various particle morphologies, though obtaining photocatalytic efficiency lower than Evonik-Degussa P25 (85% anatase + 15% rutile) [24] which is the most diffused commercial reference photocatalyst. Lin et al. [25] developed pure brookite nanosheets with structurally controlled facets working better than irregularly ones, having photocatalytic performance similar or slightly higher than P25.

In order to improve light adsorption and further extend the brookite photocatalytic activity by seizing visible light besides the UV, doping with heteroatoms (metals, non-metals or small organic molecules) [26–32] represented a promising strategy. Actually, it has been shown that nitrogen, carbon, phosphorus or sulphur doping in TiO_2 exhibits improved visible photoresponse thanks to a narrowed band gap [15, 33–37]. For instance, Feng et al [38] prepared phosphorous-doped mixed anatase-brookite TiO_2 with very high specific surface area. They showed photocatalytic efficiency 1.2 times higher than P25 under solar illumination and 3.5 times higher under visible light. Also, Brookite doped with nitrogen gave similar performance than P25 or lower when it was mixed brookite-rutile,[39] whereas Hao et al. [40] presented a nitrogen and iron doubly-doped anatase-brookite with a four-fold enhanced photocatalytic efficiency compared to P25. Finally, only a couple of materials based on carbon, nitrogen and sulphur co-doped anatase with minor amounts of brookite have been recently reported, involving complex and long syntheses even including multi-step procedures and several days of preparation [41, 42].

In this work, a carbon, nitrogen and sulphur triply-doped brookite-based photocatalyst (*d*BT) was prepared by a fast one-pot hydrothermal process, employing sol–gel chemistry and homogeneous precipitation method. The synthesis is very easy and lends itself to an eventual industrial upscaling. Furthermore, the obtained material showed an extended light absorption in the visible range and a photocatalytic activity under visible light up to eightfold higher than P25 (50-fold higher normalizing to the specific surface area). This is to the best of our knowledge the most performing brookite-based photocatalyst and in absolute terms among the best TiO_2 photocatalysts under visible light operating condition. Moreover, the material here prepared comes in the form of a barely yellow powder that is also pretty suitable for the realisation of colourless protective self-cleaning coatings.

2 Experimental

2.1 Materials Preparation

All the chemicals employed for the material preparation have been used as received, without any further purification. For the synthesis of doped brookite-based TiO_2 powder, thiourea (≥ 99%; Aldrich) and hexamethylenetetramine (HMT; ≥ 99.5%; Merck) have been respectively used as sulphur and nitrogen source, while carbon comes from their organic carbon content. In a 50 mL beaker, 6.4 g of thiourea and 2.5 g of HMT have been added in 31.25 mL of anhydrous ethanol under vigorous stirring for 10 min at room temperature. Then, the mixture has been transferred in a 250 mL Teflon lined stainless steel autoclave and added with 27 mL of Titanium(III) chloride (20% w/v solution in 2N Hydrochloric acid; Thermo Fisher Scientific) while stirring with

a glass stick in order to complete the dissolution of the last residuals of HMT and thiourea. The autoclave was fastened and placed in oven 1 h at 90 °C, 2 h at 190 °C and then took out from the oven and cooled down in ambient condition. The precipitate obtained was separated by centrifugation and washed with water and acetone three times respectively. The slightly yellow powder obtained was dried at 60 °C. Calcined samples were prepared by treating the desired amount of the material at 400, 500, 600 or 700 °C for 3 h and then by a rapid cooling down in ambient conditions out of the muffle stove. Samples are named *d*BT-NC for the non-calcined material and *d*BT-4, -5, -6 and -7 for the above calcination temperatures, respectively. No calcination was done over 700 °C because full conversion into rutile take place above this temperature [43].

2.2 Phase Structure Characterisation

The structure and phase composition of the synthesised titania powder was investigated through X-ray diffraction (XRD) technique by using a Bruker D2-Phaser powder diffractometer, equipped with a Co K-alpha ($\lambda = 1.789$ Å) X-ray source. All the diffractograms were acquired using the Bragg–Brentano 2-tetha configuration on a sample holder rotating at 15 rpm, in the 20°–80° two-theta range, with a step-size of 0.07° and a scan rate of 2°/min. The estimation of phase percentage content and crystallinity was made by Bruker Diffrac.Eva software. The mean crystallite size for brookite phase was calculated through the Scherrer equation by using the FWHM value of its XRD (121) plane reflection.

2.3 Optical Characterisation

The light absorption properties and electronic band gap of TiO$_2$ samples was estimated by Diffuse Reflectance UV–Vis Spectroscopy (DRS) in the UV–Vis region. UV–Vis absorption spectra were recorded by using a Varian Cary-500 Scan spectrophotometer equipped with an integrating sphere to collect the diffuse reflectance. The powder was pressed inside a home-made cell with a quartz window whereas a commercial white reference in Spectralon (Labsphere SBS-99-010) was used to calibrate the instrument detector. Diffuse reflectance spectra were acquired with a scan speed of 400 nm/min and are shown in the Kubelka–Munk format (KM = $(1-R)^2/2R$; R = reflectance).

Fluorescence spectra were recorded on a Fluoromax-4 spectrofluorometer (HORIBA Jobin Yvon; Edison, USA) with 150 W xenon arc lamp excitation source, respectively. The fluorescence spectra were recorded aligning the sample holder at an angle of 60° with respect to the source and using an excitation wavelength of 310 nm, whereas the quenching percentage data were calculated versus the fluorescence of the *d*BT-NC sample.

2.4 Particle Morphology, Pore-Size and Surface Area

Particle morphology and size were characterised by Transmission Electron Microscopy (TEM). The instrument (Talos F200X by FEI) was equipped with a X-FEG, working at 200 kV. TEM Images were recorded with the 4 k × 4 k CETA CMOS camera (FEI) and processed in Tecnai Imaging and Analysis software (TIA).

Nitrogen physisorption isotherms were measured with a Micromeritics TriStar 3000 equipment on samples that were pre-treated by heating at 10 °C/min to 150 °C in nitrogen flow for 14 h. The specific surface area (SSA) and the pore size distribution were determined from the Nitrogen adsorption–desorption isotherm curves at −195.8 °C (N$_2$ boiling point) by using the Brunauer–Emmett–Teller (BET) and the Barrett–Joyner–Halenda (BJH) methods, respectively.

2.5 Elemental Analysis

The sulphur content was estimated by ICP-OES analysis (SPECTRO ARCOS; SPECTRO Analytical Instruments GmbH—Germany). Samples were treated with 6 mL aqua regia (AR) overnight at 90 °C, then the AR is boiled off at 140 °C. When the samples were almost dry, 25 mL of 2% HNO$_3$ were added and left overnight at 90 °C and then injected in the spectrometer.

Nitrogen and carbon contents were determined by a Dumas combustion analyser (Fisons Instruments, model NA1500 NCS). The powders were firstly exposed to oxidation and reduction ovens at 1020 and 650 °C respectively. Then, the combustion components were separated on a 1.5 m porapack column and detected by a thermal conductivity detector (TCD).

2.6 XPS Measurements

X-ray Photoelectron Spectroscopy (XPS) spectra were acquired using a PHI 5000 VersaProbe II spectroscope (Physical Electronics, ULVAC-PHI Inc.; USA) using a monochromatic Al-Kα X-ray source with a 200 µm spot size at 50 W power. The spectra were acquired using a hemispherical analyser at the pass energy of 23.5 eV with a step size of 0.05 eV and with a photoelectron take off angle of 45°. Data analysis was done using MultiPak software V 9.7 (Physical Electronics, ULVAC-PHI Inc.; USA). Photoelectron spectra were calibrated using adventitious hydrocarbon as reference (248.8 eV).

2.7 Photocatalytic Activity

The photocatalytic performance of the materials under visible light irradiation was studied by following the

photodegradation of methylene blue (MB) ($\geq 95\%$; Aldrich) intended as a model dye. For every sample, a 4 mg/mL aqueous suspension was prepared in a 100 mL beaker by adding titania powder to water followed by 1 min treatment in ultrasonic bath (Branson, model 2800). Then, a MB aqueous solution was added to obtain a final concentration of 2.6 mg/L. The titania suspension was left 30 min in the dark under vigorous stirring in order to let MB absorb on titania surface. Therefore, the suspension under continuous stirring was illuminated with a collimated visible light beam (round geometry, 1 cm^2 area) by using a 150 W Xe-lamp (ORIEL, model 67005) whose irradiance was filtered under 400 nm through a long-pass coloured glass filter (THORLabs, FGL400S). No transmitted light was observed. After any established interval of time, part of the suspension was taken and centrifuged to eliminate titania powder and the residual absorbance of MB was measured by an UV–Vis spectrophotometer (Agilent Cary 60 UV–Vis). The intensity of the MB main absorbance peak at 663 nm has been reported against time in order to follow the MB photocatalytic degradation operated by the titania sample. As a reference, the same experiment was conducted by using Evonik-Degussa P25 titania (Aldrich, Evonik-Degussa Aeroxide® P25). An equal concentration solution of MB alone was also irradiated for 30 min with visible light in the same condition in order to assay photolysis and no measurable MB degradation was detected.

Total Organic Carbon (TOC) measurements ware performed on P25 and dBT-7 samples prepared as above, with MB added to obtain 20 ppm starting TOC, then irradiated for 24 h using a solar simulator with 35 mm round beam and 1 sun of irradiance (Albeit Technologies, Model 10500), whose IR fraction was attenuated by a water filter. Then, suspensions were centrifuged in order to separate titania powder and residual TOC was measured (Shimadzu 5050A TOC Analyser equipped with ASI 5000A autosampler).

2.8 Electrochemical Determination of Band Edge Positions

The conductive band edge was determined by applying a photo-electrochemical methodology described elsewhere [44, 45]. In a three-necked round flask, 50 mg of sample powder were suspended in 50 mL of potassium nitrate (Fisher Scientific, 99 + %) 0.1 M with the help of 1 min ultrasonic bath treatment. The obtained suspension was bubbled with dry nitrogen for 30 min, then 6 mg of methyl viologen dichloride (Aldrich, 98%) were added and further 10 min of nitrogen were bubbled again. Next, the potential of a 1 cm^2 platinum plate electrode was measured at different pH with respect to an aqueous Ag/AgCl, NaCl 3 M reference electrode by using a commercial multi-meter. The measurements were made under continuous stirring

and nitrogen flow and while irradiating the flask with a 75 W Xe-lamp (Photon Technological International). The pH of the system was adjusted in the range 1–12 by using sodium hydroxide or hydrochloric acid 1 M and monitored by a glass-electrode pH-meter (Hanna Instruments). The valence band was calculated by using the optical band gap value.

3 Results

3.1 X-ray Diffraction Analysis on Material Structure and Phase Composition

The XRD diffractograms for all of the dBT samples are reported in Fig. 1. In order to further increase crystallinity and photocatalytic activity, the obtained powder was calcined at different temperature and diffractograms show how crystallinity and phase composition (Table 1) evolved with the heat treatment. The non-calcined (dBT-NC) material displayed a composition with predominant brookite content, lower anatase and minor rutile percentage. As expected, by increasing the calcination temperature a decrease of the peak FWHM indicated an improvement of the material crystallinity going from about 78% up to 91% beside the growth of the crystallite size (inset in Fig. 7). The rutile phase percentage grew whereas anatase and brookite slightly decreased. At the highest calcination temperature (dBT-7) brookite was the main phase with about 70% content, while anatase and rutile were about 21 and 10%, respectively.

Also, it is worth to note that no peaks related to C, N and S species could be observed in the XRD diffractograms. This suggests that dopant elements were incorporated into the TiO$_2$ lattice, occupying titanium and/or oxygen substitutional sites or located at the interstitial sites.
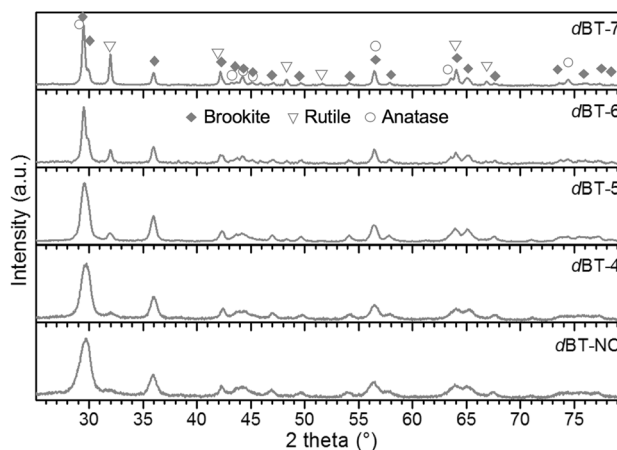

Fig. 1 XRD analysis for all the investigated samples

Table 1 XRD Phase composition and crystallinity, specific surface area and pore volume for *d*BT samples

Sample name[a]	Brookite %	Anatase %	Rutile %	Crystallinity %	SSA m^2/g	Pore volume cm^3/g
*d*BT-NC	74.5	22.1	3.5	78.4	131.3	0.62
*d*BT-4	74.2	22.4	3.4	80.9	82.2	0.60
*d*BT-5	74.5	22.6	2.9	86.9	56.0	0.53
*d*BT-6	72.9	22.0	5.2	88.5	31.3	0.33
*d*BT-7	68.7	20.7	10.5	91.6	9.4	0.12
P25	–	~85	~15	–	55.4	0.22

[a]Suffix—NC stays for non-calcined sample, while suffixes −4 up to −7 stay for samples calcined from 400 °C up to 700 °C respectively

3.2 Transmission Electron Microscopy Analysis of Material Nanoparticle Size and Morphology

The morphology of the *d*BT nanoparticles was characterised through TEM analysis (Fig. 2) that also confirmed the size increase already pointed out by the XRD. Micrograph in Fig. 2a presents the morphology of the noncalcined brookite nanoparticles. These are characterised by two different shapes: round nanoparticles with size around 10 nm as well as elongated nanoparticles about 10 nm in width and 50 nm in length. By the calcination process, rod-like particles disappeared and the size of the round shaped particles increased as shown in Fig. 2b, c. Indeed, sample *d*BT-5 has round multifaceted particles with diameter between about 10 nm and 50 nm while some large pores cross the particle body. By calcination at 700 °C (Fig. 2c), the particle preserved a round multifaceted geometry and further increased their size, with diameters in the 20–200 nm range with a limited number of smaller particles.

3.3 Nitrogen Adsorption Measurements for Surface Area and Pore Size Determination

In accordance with TEM results, the growth of the particle size due to the thermal sintering affected both the material SSA and its porosity, as revealed by the N$_2$-adsorption analysis (Fig. 3). The adsorption isotherms display a type IV shape, indicating a mesoporous nature [46] for all the samples. By increasing the calcination temperature there is a considerable decrease in the pore volume and in the SSA, the latter going from 131.3 m^2/g for *d*BT-NC down to 9.4 m^2/g for *d*BT-7 (Table 1). As for the pores dimension, it slightly decreased from about 3 nm to about 2 nm, as shown in the pore size distribution (Fig. 3, inset).

3.4 X-ray Photoelectron Spectroscopy Analysis of *d*BT Particle Surface

Since photocatalysis is a surface phenomenon, we investigated the surface chemical composition and the state of dopant elements by XPS. The obtained surface composition of the samples is compared with that of commercial undoped P25 titania (Table 2). Besides titanium and oxygen,
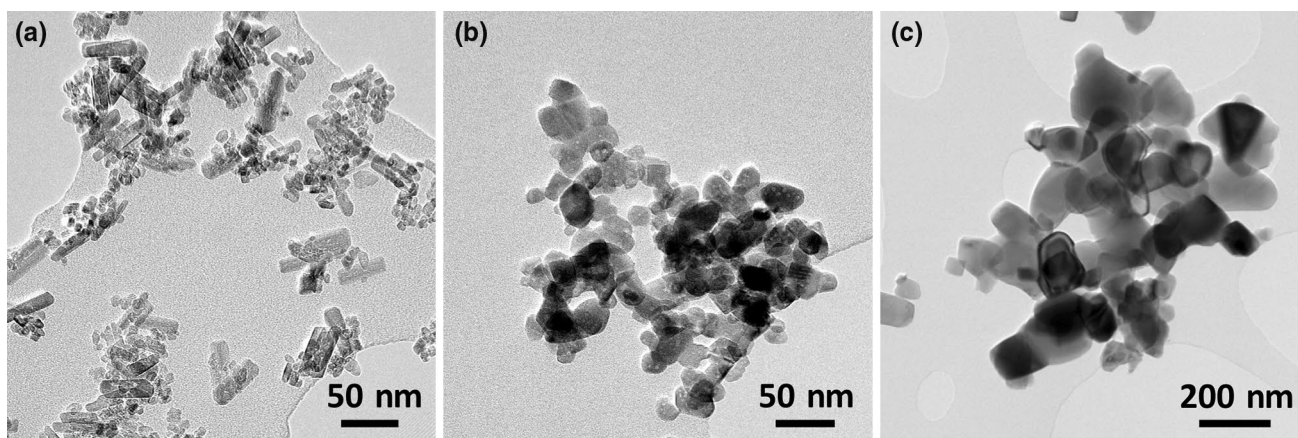

Fig. 2 TEM micrographs for samples *d*BT-NC (**a**), *d*BT-5 (**b**) and *d*BT-7 (**c**)
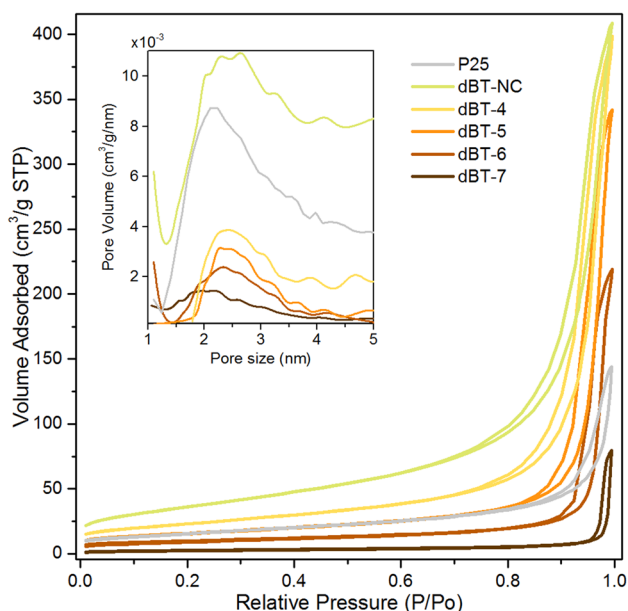
Fig. 3 Nitrogen adsorption–desorption isotherms; the inset shows pore size distribution

Table 2 Surface composition measured by XPS (at.%)

	Titanium	Oxygen	Carbon	Nitrogen	Sulphur
P25	28.5	66.8	4.7	–	–
dBT-NC	26.8 (33.1)	63.4 (66.2)	6.7 (0.5)	2.5 (0.1)	0.5 (0.1)
dBT-4	26.2	64.6	6.8	2.0	0.5
dBT-5	26.4	63.7	7.3	2.0	0.6
dBT-6	26.7	64.7	6.5	1.6	0.5
dBT-7	26.5	63.6	8.5	1.0	0.3

Values in brackets for sample dBT-NC are for bulk composition as measured by Dumas combustion and ICP-OES

P25 also contains some adventitious carbon adsorbed from the atmosphere while in the case of the doped samples, an increased carbon content as well as nitrogen and sulphur were detected because of the doping. In the case of dBT-NC sample, the bulk composition was also measured by Dumas combustion and ICP-OES (Table 2) and compared with the surface composition obtained by XPS. Interestingly, the surface dopant atomic percentage (at.%) is bigger than the bulk one suggesting that dopant atoms are likely able to migrate outward during the synthesis, determining the formation of particles having a sort of doped surface. By calcining the materials at increasing temperature, the total amount of doping is constant while the carbon generally grew from 6.7% up to 8.5% suggesting a progressive displacement of carbon toward the particles surface. Conversely, the nitrogen amount decreases from 2.5% down to 1% probably because it may form oxidised volatile species that leave the material

[47]. Quite the same applies for sulphur, which maintains a concentration of about 0.5% with a slight decrease to 0.3% at the highest temperature.

In order to investigate the chemical state of dopants, high resolution XPS spectra were acquired for each dBT sample (Fig. 4). The C 1s spectra can be fitted by four components respectively at binding energies (BE) of: 284.8 eV for C–C bonds of adventitious carbon species; 286.5 and 288.5 eV respectively for C–O and C=O or O–C=O bonds in carbonate species [48, 49]; about 282 eV for C–Ti bonds from carbon atoms substituting oxygen sites in the TiO_2 lattice [48, 50]. Notably, the peak at 288.4 eV could also be ascribed to C substitution at Ti sites giving a Ti–O–C structure [42]. Moreover, the weak C–Ti signal tends to disappear with increasing temperature probably because of carbon oxidation during the calcination while the C–O peak for dBT-7 is the most intense indicating that particle surface in this sample is richer in oxidised carbon species.

The N 1s spectra may be fitted by two broad peaks at about 406–409 eV and 397–403 eV. According to literature, signals in this latter region can be associated to interstitial nitrogen doping in Ti–O–N and Ti–N–O bonds [48, 49, 51–56] as well as to substitutional anionic doping in O–Ti–N bonds where N atoms lies in the oxygen sites [56]. The other peak at higher BE is ascribed to oxidised nitrogen species like nitrate, indicating that part of nitrogen atoms underwent oxidation at the particles surface. As to the sulphur, the S 2p spectrum for the sample dBT-NC displays a peak at 164 eV
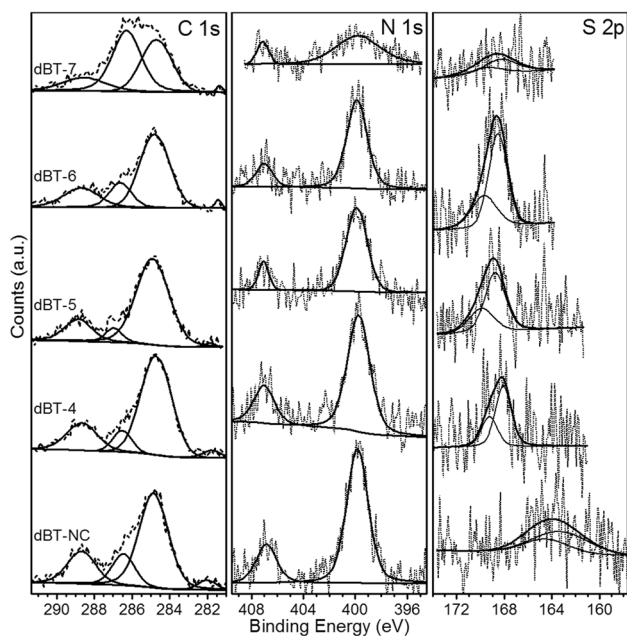

Fig. 4 High-resolution XPS spectra of C-1s, N-1s and S-2s for dBT samples (dotted line: original spectrum; solid line: fitted peaks; in the S2p panel thinner solid lines are for the S-2p1/2 and S-2p3/2 spinorbit doublets)

that can be assigned to anionic dopant S^{2-} substituted in oxygen sites and involved in Ti–S bonds [49]. Interestingly, during the calcination the sulphur underwent oxidation [36] and its peak shifted at higher BE. Indeed, in all the calcined samples the S 2p peak pins at about 168.5 eV suggesting the formation of S^{6+} dopant species in Ti sites (Ti–O–S bonds) [48, 51]. This oxidative process could have been favourite also by the fact that S^{2-} anionic doping is difficult to obtain because of the larger ionic radius of S^{2-} (1.7 Å) compared to that of O^{2-} (1.22 Å) [57].

Figure 5 reports the high resolution XPS spectra of Ti and O. These signals are characterised by a peak shift of all *d*BT samples toward lower BE compared to the P25 reference, endorsing the dopant incorporation. Actually, the lower BE values for Ti 2p in *d*BT samples may be ascribed to a higher electron density on Ti^{4+} due to the different interaction with surrounding ions containing besides oxygen, also the less electronegative dopant elements [58, 59]. As for the oxygen, the O 1s signal for the commercial titania can be fitted by an intense peak at about 530 eV usually assigned to Ti–O bond and a weak peak at 531.5 eV relative to C–O bonds with adventitious carbon on the surface. Seemingly, the O 1s spectra for *d*BT samples showed two components that can be attributed to the same two bonds. However, in accordance with the literature and considering the presence of dopant N atoms from the analysis of N 1s spectra, it is possible to ascribe the higher energy component not only to C–O but even to Ti–O–N bonds [49, 60]. Moreover, the downward

shift of O 1s signals for *d*BT samples compared to P25 may also be connected with the presence of less electronegative dopant elements that increase electron density on oxygen atoms [49, 60].

3.5 Diffuse Reflectance Spectra and Band Gap Determination of *d*BT

In order to evaluate the doping effect on the extension of the optical absorbance in the visible range, DRS measurements were accomplished on all the prepared materials. The spectra are compared with that of the Evonik-Degussa P25. Interestingly, as reported in Fig. 6a, all of the samples showed a reflectance considerably lower (i.e. higher absorbance) than P25 all across the visible range, *d*BT-7 sample being the best.

Furthermore, in the inset of the same figure the reflectance data are depicted as the fraction of solar radiation that P25 and *d*BT-7 are able to absorb from the typical AM1.5G solar spectral irradiance. By considering the full range NUV-Vis-NIR (280–900 nm), P25 is able to absorb about 14% of the solar radiance, while the sample *d*BT-7 absorbs about 22%. In total, the sample *d*BT-7 absorbs 53% more light than P25. More importantly, by taking into consideration only the visible range of radiation (390–700 nm) the difference between *d*BT-7 and P25 becomes even larger. Indeed, *d*BT-7 absorbs 100% more light than P25, the former being able to absorb about 20% of the solar spectrum whereas the latter only about 10%.

What above is also connected with a narrowed energy gap of the synthesised doped materials. By transforming reflectance data through the Kubelka–Munk function (F(R$_\infty$)) and plotting it as a Tauc's plot (Fig. 6b) for an indirect semiconductor, it is possible to extrapolate from the last linear segment of the curve the band gap energy values for the synthesised materials. As for P25, the figure shows a band gap of 3.58 eV and a long Urbach's tail at lower values. Notably, in the case of *d*BT samples this value is fairly lower compared to P25. Indeed, band gap was reduced to about 3.08 eV for *d*BT samples, the curves having a linear behaviour till lower values.

Furthermore, the UV–Vis spectra and particularly Tauc's plots in proximity of the band gap energies (between 350 and 400 nm and 3–3.5 eV) reveal a gradually increase in intensity from *d*BT-NC to *d*BT-7. This may be related to a growth in the density of states (DOS) of the orbitals around the band gap providing more electrons available to be excited by visible light. Actually, among TiO$_2$ polymorphs the brookite displays the highest DOS around the band gap [12, 61]. Moreover, this gradually increase of DOS more likely derives from the increasing crystallinity that follows the heat treatment (Table 1) leading to an extended orbital overlap [62, 63]. Another reason could lie yet in the variation of the
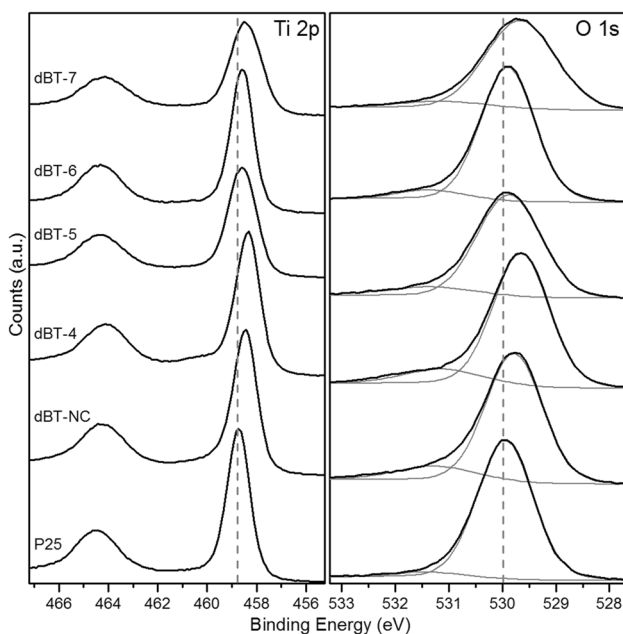
Fig. 5 High-resolution XPS spectra of Ti 2p$_{3/2}$ and 2p$_{1/2}$ doublet and O 1s for undoped P25 and *d*BT samples (dashed lines are to better display the peak shift compared to P25; gray lines in O 1s pane fit oxygen components)
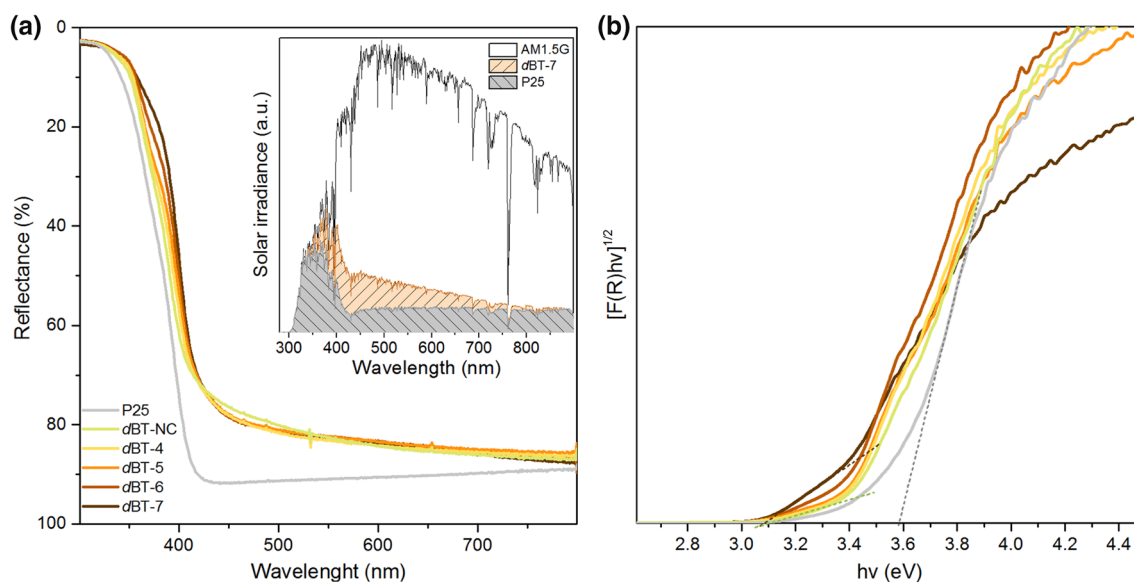
Fig. 6 Diffuse reflectance UV–Vis spectra (**a**) and Tauc's plot (**b**) comparing the prepared samples with P25 titania. The inset in **a** compares the portions of solar radiation that P25 and bBT-7 are able to absorb

doping percentage with calcination, as the carbon amount grows from 6.7 to 8.5% (Table 2) increasing the contribution of carbon orbitals in the formation of the valence band, though the total doping percentage remain quite constant at about 9.5% for all the samples.

3.6 Fluorescence Spectroscopy Study on Electron–Hole Recombination Degree

Since electrons and relative holes need to separately reach the surface to trigger photocatalysed reactions, the degree of charge recombination is an important factor and was investigated by fluorescence spectroscopy. Figure 7 reports the fluorescence spectra for all the samples, showing that their emission intensity gradually decreased from *d*BT-NC to *d*BT-7. As the fluorescence emission arises from the electron–hole recombination, the progressive fluorescence quenching in Fig. 7 corresponds to a reducing charge recombination degree with the calcination treatment. Moreover, fluorescence quenching correlates with the increase in the crystal size of the predominant brookite phase (Fig. 7, inset).

3.7 Characterisation of the Electronic Structure

The electronic structures of P25 and *d*BT samples (Fig. 8) were determined and compared, because the valence band (VB) and conductive band (CB) positions may be of paramount importance in efficiently driving a photocatalytic process. In particular, the VB position was determined by XPS (Fig. 8a, b) obtaining the CB position by adding the optical band gap values (Fig. 8b). These energy level positions
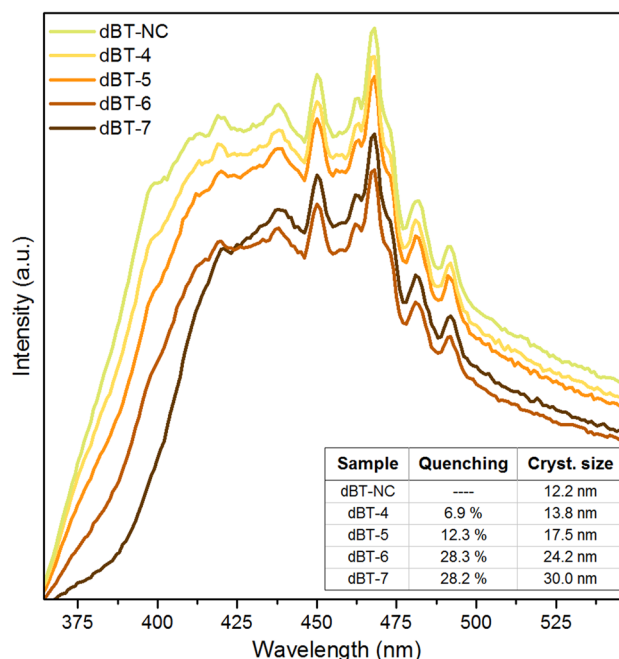

Sample	Quenching	Cryst. size
dBT-NC	----	12.2 nm
dBT-4	6.9 %	13.8 nm
dBT-5	12.3 %	17.5 nm
dBT-6	28.3 %	24.2 nm
dBT-7	28.2 %	30.0 nm

Fig. 7 Fluorescence spectra of *d*BT sample; the inset report the luminescence quenching percentage in relation with the brookite crystallite size calculated from XRD data

were crosschecked by electrochemical measurement of CB [44, 45] obtaining a very good agreement (Fig. 8b, values in brackets). Interestingly, Fig. 8a, b show that the *d*BT samples present an upward extension of the VB with respect to P25, while CB (Fig. 8b) remained unaffected for sample up to *d*BT-6, thus evidencing a substantial band gap narrowing.
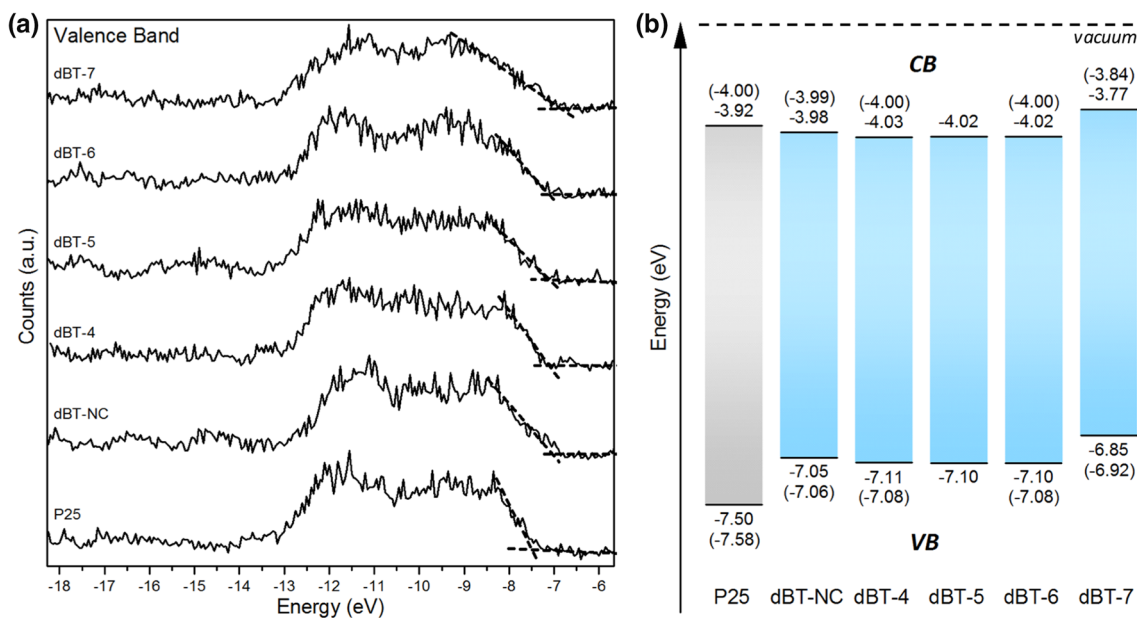
Fig. 8 **a** XPS VB region; dashed lines help to pinpoint the VB upper edge. **b** Energy bands diagram with CB and VB positions from XPS while in brackets are the values electrochemically measured (it was not possible to obtain these values for *d*BT-5); shaded colour is the band gap region

A special case is *d*BT-7, where both VB and CB resulted upshifted.

Interestingly, Fig. 8 shows that the energy-gap narrowing revealed by DRS measurements in all the doped samples arises primarily from the upward extension of the VB with respect to P25. According to Tang et al. [33] the reason might be that the atomic orbitals of these non-metal dopants (i.e. N 2p, S 3p, and C 2p) have higher energy than oxygen in TiO$_2$. This would form a new extended and mixed VB in place of the native pure O 2p band, which reduces the band-gap energy without affecting the CB level. Similar results were published for N-doped TiO$_2$ reporting band gap narrowing and enhanced photocatalysis on the basis of N atoms substitution in O-site and the related N 2p and O 2p orbital mixing. The same was reported for both anionic and cationic S-doping, which lead to band gap narrowing thanks to VB extension from S 3p and O 2p mixing [47]. While for substitutional doping the band gap narrowing via VB extension from mixing orbitals is the most common interpretation, it was instead reported that interstitial doping leads generally to discrete energy levels lying above the VB inside the band gap, called mid-gap states [64]. In agreement with this and also with the reported XPS data, doping in *d*BT samples seems to be mainly of a substitutional nature. Indeed, XPS spectra of elements are compatible with substitutional doping and VB (Fig. 8a) do not show any discrete energy level above the VB upper edge, while showing an extended range compared to the undoped P25.

Hence, while the samples with similar phase composition maintain a quite similar VB-CB energy values, *d*BT-7

shows upward shifted band positions. Likely, this shift could be mainly related to the noticeable change in composition for *d*BT-7 whose rutile content is more than doubled, rather than to any variation in the doping at.% that would primarily affects the VB [33].

3.8 Photocatalytic Activity of P25 and *d*BT: Characterisation and Comparison

Figure 9 reports photocatalytic degradation of the MB in aqueous solution under visible light irradiation ($\lambda > 400$ nm). The MB is used as a model environmental organic pollutant. These experiments are intended to ascertain if the improved optical and electronic properties of the material are able to induce an enhanced photocatalytic activity once in a visible light illuminated environment (sun or artificial source).

As usually reported in literature, the photocatalytic degradation of MB is spectroscopically assessed by following the abatement of its maximum absorbance peak at 663 nm against the illumination time. As above for light absorption, the kinetic profiles of the MB degradation by the samples are posed in comparison with the one coming from P25 (Fig. 9a). The curves show that the non-calcined sample and *d*BT-4 gave a slower degradation with respect to P25 while the samples calcined at higher temperatures were progressively faster, with *d*BT-7 that showed a very swift reaction rate (Fig. 9b). Indeed, MB photodegradation by P25 proceeds with a rate constant of about 0.005 min^{-1} with a run ending after about 1200 min, while *d*BT-7 shows a larger rate constant of about 0.041 min^{-1} and a degradation
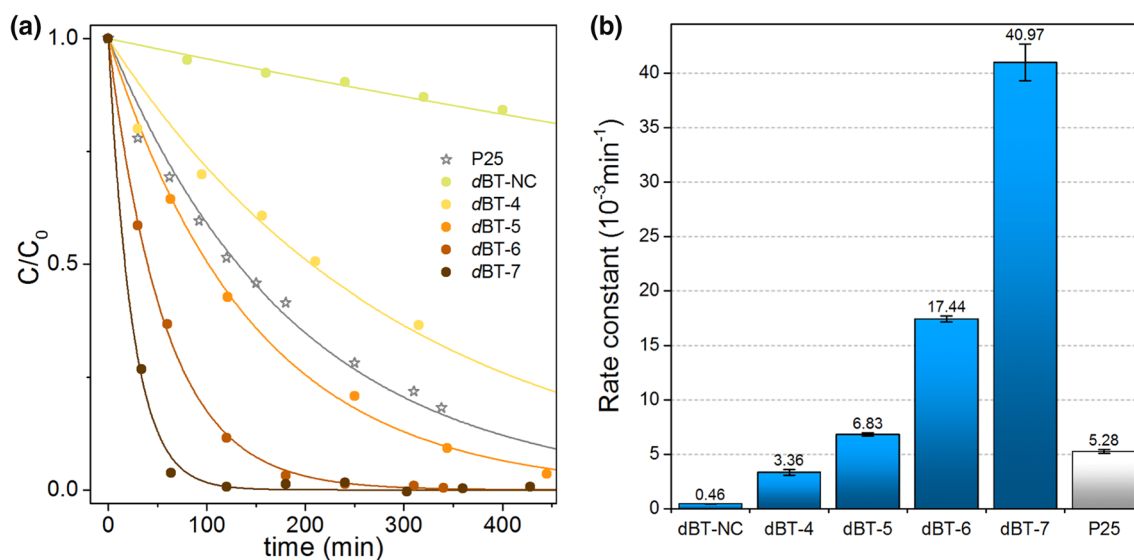
Fig. 9 **a** Photodegradation trend and **b** related rate constants for the MB under visible light using *d*BT samples and P25. Data points in **a** are fitted by considering a 1st order kinetics

run ending in about 150 min. Therefore, *d*BT-7 acts about 8 times faster than P25 under visible light irradiation (see Fig. 9b).

Finally, for some application different from self-cleaning coating, e.g. water remediation, it is important not only the dye decolouration but also the reduction of the total organic carbon (TOC). For this reason, we also measured the residual TOC content in completely decoloured MB solutions, obtained by irradiating with a solar simulator emitting in the range 300–1600 nm. It resulted that by using the P25 a TOC reduction of about 13% was achieved while *d*BT-7 photocatalyst gave a better performance reaching the 40% of TOC abatement.

4 Discussion

The C,N,S-doped brookite-based titania nanoparticles were synthesised following a sol–gel route by homogeneous precipitation in a solvo-thermal process. $TiCl_3$ was employed as titanium precursor due to its reduced reactivity and because it fosters the formation of brookite structure [65–67] while HMT and thiourea were used as precipitating agents and as a source for carbon, nitrogen and sulphur doping elements [36, 41, 67]. Initially, at temperatures above 70 °C these compounds hydrolyse to homogeneously generate ammonia across the solution leading to the precipitation of amorphous TiO_2 [39, 68]. Subsequently, the solvo-thermal treatment at higher temperature and pressure yields higher crystallinity and allows the incorporation of dopants inside the structure leading to well-crystallised doped brookite. This synthetic procedure led to the precipitation of a slightly

yellow powder, composed by thin nanoparticles of crystalline brookite-based TiO_2 with a very high specific surface area of 131.3 $m^2 g^{-1}$. Composition analysis showed that the dopant species are localised especially on the outer layers of the material, determining the formation of particles having a sort of doped surface.

The photocatalytic activity of *d*BT under visible light (Fig. 9a) showed a gradual increase of performance with the calcination temperature, with *d*BT-7 standing out showing an apparent MB photodegradation rate 8-times faster than P25 (Fig. 9b). However, this data becomes even more outstanding if considered with respect to the decreasing surface area of *d*BT samples (Table 1) after calcination. Indeed, P25 has a SSA of 55.4 $m^2 g^{-1}$, while *d*BT-7 presents a far lower value of about 9 $m^2 g^{-1}$ yet showing a much better photocatalytic activity. If, as often reported in literature, the apparent rate of MB photodegradation is normalized by the SSA in order to consider that all the surface area takes part in the photocatalytic reaction [69], it comes out 0.46 mg m^{-2} min^{-1} for *d*BT-7 and only about 0.01 mg m^{-2} min^{-1} for P25. Hence, visible light photocatalytic activity of *d*BT-7 is nearly 50-fold higher than P25.

It has to be noted that in addition to the photocatalytic degradation MB could be also consumed through a minor alternative mechanism (independent from the photocatalyst) in which the MB adsorbed on the titania surface is photoexcited, injects an electron into the titania CB and decomposes by oxidation [70, 71]. The contribution of this alternative mechanism is however expected to be larger for the P25 than *d*BT-7, since the former has a greater surface area (Table 1) and a lower LUMO level (better electron acceptor, Fig. 8b) than the latter. Thus, the higher photocatalytic

performance of *d*BT-7 with respect to P25 could be at most underestimated.

The rationale for the enhanced photocatalytic activity with respect to P25 and its progressive increase with the calcination temperature (Fig. 9) is of course complex and different reasons can be put forward. First, the larger amount of light exploited by *d*BT due to the reduced band gap and to the marked increase of absorption all along the visible range (Fig. 6) could be one main contribution to the higher photocatalytic activity. Still, we should also consider the growing light absorption from *d*BT-NC to *d*BT-7 (Fig. 6) as a gradually contributing factor, though this contribution is considered to be small. However, the better light absorption is not enough for samples *d*BT-NC and *d*BT-4, which show yet lower activity than P25. These are probably paying a low crystallinity degree. Indeed, as shown in Fig. 10, a further important contribution to the photocatalytic activity come from the gradual increase in crystallinity and crystallite size with calcination (Table 1).

Besides contributing to the increasing light adsorption and DOS, a higher crystallinity entails a parallel enhancement in the lifetime and diffusion length of photo-generated electrons and holes. In this way, charges are able to move faster and to reach the reaction sites on the particle surface before recombination, hence in a larger number [72]. This hypothesis has been verified by fluorescence measurements [73, 74] (Fig. 7), where the quenching percentage increased with the crystallite size from *d*BT-NC to *d*BT-7, indicating a reducing electron–hole recombination (Fig. 10; inset in Fig. 7). However, the crystallinity enhancement cannot explain the rate constant increase from *d*BT-6 to *d*BT-7 since there is 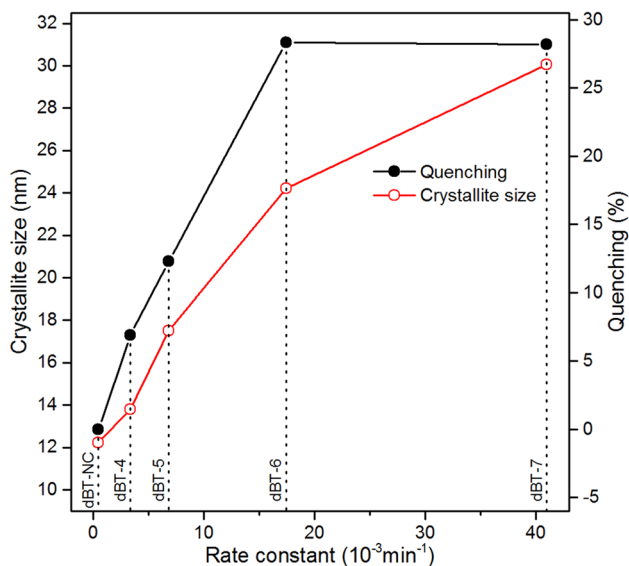not any further gain in quenching percentage in this range, as shown in Fig. 10. Interestingly, the highest C–O and total carbon doping percentage (Table 2; Fig. 4) could be one reason for the additional increase of photocatalytic activity in *d*BT-7, as it is known that carbon in C–O and C=O structure is able to enhance visible light absorption and photocatalytic activity [48, 50]. Moreover, by looking at phase compositions, the sample *d*BT-7 seems to receive a further boost in photocatalytic activity by the increase of its rutile content, which doubled passing from about 5 to 10.5% (Table 1). As shown by the characterisation of the electronic structure (Fig. 8), this sudden change in composition is responsible for an upward shift of band positions. Interestingly, it has been reported that brookite has a strong affinity with O$_2$ in water [69] and this band shift entails a better energy alignment with respect to its reduction potential (Fig. 11) [75, 76].

Actually, the oxygen reduction is a very important process because it generates the reactive O$_2^{\bullet-}$ radical that is fundamental in all the atmospheric photocatalytic processes. Furthermore, besides being a strong oxidant itself, O$_2^{\bullet-}$ is directly involved in the formation of H$_2$O$_2$ and OH$^\bullet$, which are powerful oxidative agents in the degradation of environmental pollutant (see box in Fig. 11) [77].

In the case of *d*BT-7, the difference between the CB and the reduction potential of O$_2$/O$_2^{\bullet-}$ and H$_2$O$_2$/OH$^\bullet$ is markedly bigger than for the other materials including P25. The larger potential difference may act as an increased driving force that better promotes the photoexcited electron transfer
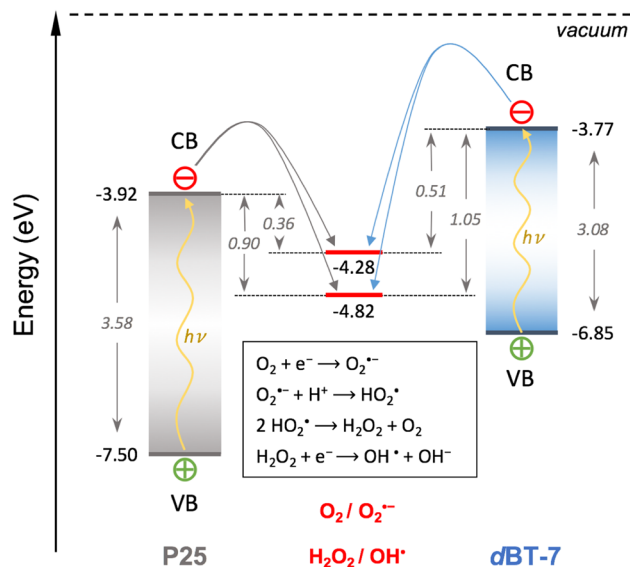

Fig. 10 Relationships between MB photodegradation rate constant, Brookite crystallite size and Quenching

Fig. 11 Schematic of the proposed mechanism for enhanced efficiency of photocatalytic process; formation of O2•⁻ and OH• radicals via oxygen reduction in water by P25 and *d*BT-7 samples (note that drawing is not on scale to show better the mechanism). In the inset, the reactions yielding the reactive radicals are reported

from the *d*BT-7 to the molecular oxygen, boosting the generation of the reactive $O_2^{\bullet-}$ and $OH^\bullet$ radicals.

Finally, from the experimental data it seems that a predominant composition in brookite phase would be important for higher visible light photocatalytic activity. As a matter of fact, P25 that only contains anatase and rutile shows a well lower performance and there is a number of published studies showing how favourable is the presence of brookite polymorph in the composition of an effective photocatalyst [43, 78–80]. Yet, another possible contributing factor for this fruitful phase interplay could also lie in the formation of heterojunctions at the interface between domains of different phases yielding electron–hole improved separation, as already demonstrated for other systems [81–83].

5 Conclusions

Brookite titania polymorph has been taken into consideration because of its promising properties in photocatalysis. A very effective C,S,N-doped brookite-prevalent mesoporous photocatalyst has been prepared via a rapid and easy one-pot sol–gel synthesis and its electro-optical and photocatalytic properties were compared to the commercial P25 TiO_2 reference.

The synthesised materials displayed enhanced light absorption all across the visible range (100% gain) and a 0.5 eV band gap narrowing due to the upward extension of VB by doping. The photocatalytic activity improved in parallel with absorbance and was further optimised at higher calcination temperature by the increasing of crystallinity and amount of carbon species as well as by the rutile percentage growth that caused the VB and CB upshift. Importantly, the enhanced crystalline order (reduced electron–hole recombination degree) may balance the loss in the SSA after the heat treatment. As a consequence, the sample *d*BT-7 showed the best performance (up to 50-times than P25 TiO_2) for brookite-based photocatalyst resulting among the top-performing TiO_2 catalysts under visible light.

In conclusion, the fine tuning of crystal quality and carbon doping at surface together with the phase composition balance with high brookite content seems to be key factors for achieving top performance in TiO_2 photocatalysts. Usefully, this material comes in the form of a barely yellow powder that is also pretty suitable for the realisation of colourless protective self-cleaning coatings, but it also may find successful applications in photoelectrochemical water-splitting devices as well as in the photocatalytic removal of environmental organic pollutants from air or water bodies.

Compliance with Ethical Standards

Conflict of interest The authors declare that they have no conflict of interest.

References

1. Zhang Q, Huang Y, Xu LF, Cao JJ, Ho WK, Lee SC (2016) ACS Appl Mater Interfaces 8:4165
2. Faraldos M, Kropp R, Anderson MA, Sobolev K (2016) Catal Today 259:228
3. Banerjee S, Dionysiou DD, Pillai SC (2015) Appl Catal B 176:396
4. Ganesh VA, Raut HK, Nair AS, Ramakrishna S (2011) J Mater Chem 21:16304
5. Zhang W, Jia B, Wang Q, Dionysiou D (2015) J Nanopart Res 17:1
6. Romão J, Barata D, Ribeiro N, Habibovic P, Fernandes H, Mul G (2017) Environ Pollut 220:1199
7. Fujishima A, Honda K (1972) Nature 238:37
8. Acar C, Dincer I, Naterer GF (2016) Int J Energy Res 40:1449
9. Jafari T, Moharreri E, Amin AS, Miao R, Song W, Suib SL (2016) Molecules 21:900
10. Ampelli C, Centi G, Passalacqua R, Perathoner S (2016) Catal Today 259:246
11. Guo Q, Zhou C, Ma Z, Ren Z, Fan H, Yang X (2016) Chem Soc Rev 45:3701
12. Landmann M, Rauls E, Schmidt WG (2012) J Phys Condens Matter 24:195503
13. Luttrell T, Halpegamage S, Tao J, Kramer A, Sutter E, Batzill M (2014) Sci Rep 4:4043
14. Kim W, Tachikawa T, Moon G-h, Majima T, Choi W (2014) Angew Chem Int Ed 53:14036
15. Di Paola A, Bellardita M, Palmisano L (2013) Catalysts 3:36
16. Banerjee S, Gopal J, Muraleedharan P, Tyagi K, Raj B (2006) Curr Sci 90:1378
17. Wunderlich W, Oekermann T, Miao L, Hue NT, Tanemura S, Tanemura M (2004) J Ceram Process Res 5:343
18. Shibata T, Irie H, Ohmori M, Nakajima A, Watanabe T, Hashimoto K (2004) Phys Chem Chem Phys 6:1359
19. Koelsch M, Cassaignon S, Guillemoles JF, Jolivet JP (2002) Thin Solid Films 403–404:312
20. Štengl V, Králová D (2011) Mater Chem Phys 129:794
21. Reyes-Coronado D, Rodriguez-Gattorno G, Espinosa-Pesqueira ME, Cab C, de Coss R, Oskam G (2008) Nanotechnology 19:145605
22. Mattsson A, Österlund L (2010) J Phys Chem C 114:14121
23. López-Muñoz MJ, Revilla A, Alcalde G (2015) Catal Today 240:138
24. Ohtani B, Prieto-Mahaney OO, Li D, Abe R (2010) J Photochem Photobiol A 216:179
25. Lin H, Li L, Zhao M, Huang X, Chen X, Li G, Yu R (2012) J Am Chem Soc 134:8328
26. Etacheri V, Di Valentin C, Schneider J, Bahnemann D, Pillai SC (2015) J Photochem Photobiol C 25:1
27. Fu C, Gong Y, Wu Y, Liu J, Zhang Z, Li C, Niu L (2016) Appl Surf Sci 379:83

28. Tosoni S, Fernandez Hevia D, Gonzalez Diaz O, Illas F (2012) J Phys Chem Lett 3:2269
29. Reddy PAK, Reddy PVL, Kim K-H, Kumar MK, Manvitha C, Shim J-J (2017) J Ind Eng Chem 53:253
30. Pikuda O, Garlisi C, Scandura G, Palmisano G (2017) J Catal 346:109
31. Ozer Y, Shin L, Felten Y, Oladipo A, Pikuda H, Muryn O, Casiraghi C, Palmisano C G (2017) J Environ Chem Eng 5:5091
32. Lei XF, Zhang ZN, Wu ZX, Piao YJ, Chen C, Li X, Xue XX, Yang H (2017) Sep Purif Technol 174:66
33. Tang X, Li D (2008) J Phys Chem C 112:5405
34. Pelaez M, Nolan NT, Pillai SC, Seery MK, Falaras P, Kontos AG, Dunlop PSM, Hamilton JWJ, Byrne JA, O'Shea K, Entezari MH, Dionysiou DD (2012) Appl Catal B 125:331
35. Asahi R, Morikawa T, Ohwaki T, Aoki K, Taga Y (2001) Science 293:269
36. Ohno T, Akiyoshi M, Umebayashi T, Asai K, Mitsui T, Matsumura M (2004) Appl Catal A 265:115
37. Etacheri V, Michlits G, Seery MK, Hinder SJ, Pillai SC (2013) ACS Appl Mater Interfaces 5:1663
38. Feng H, Zhang M-H, Yu LE (2013) J Nanosci Nanotechnol 13:4981
39. Yin S, Aita Y, Komatsu M, Wang J, Tang Q, Sato T (2005) J Mater Chem 15:674
40. Hao H, Zhang J (2009) Microporous Mesoporous Mater 121:52
41. El-Sheikh SM, Zhang G, El-Hosainy HM, Ismail AA, O'Shea KE, Falaras P, Kontos AG, Dionysiou DD (2014) J Hazard Mater 280:723
42. Zhang G, Zhang YC, Nadagouda M, Han C, O'Shea K, El-Sheikh SM, Ismail AA, Dionysiou DD (2014) Appl Catal B 144:614
43. Mutuma BK, Shao GN, Kim WD, Kim HT (2015) J Colloid Interf Sci 442:1
44. Beranek R (2011) Adv Phys Chem 2011:1
45. Roy AM, De GC, Sasmal N, Bhattacharyya SS (1995) Int J Hydrog Energy 20:627
46. Thommes M, Kaneko K, Neimark AV, Olivier JP, Rodriguez-Reinoso F, Rouquerol J, Sing KSW (2015) Pure Appl Chem 87:1051
47. Etacheri V, Seery MK, Hinder SJ, Pillai SC (2012) Inorg Chem 51:7164
48. Wang P, Yap P-S, Lim T-T (2011) Appl Catal A 399:252
49. Wang Y, Huang Y, Ho W, Zhang L, Zou Z, Lee S (2009) J Hazard Mater 169:77
50. Gu DE, Lu Y, Yang BC, Hu YD (2008) Chem Commun 21:2453
51. Rengifo-Herrera JA, Pierzchała K, Sienkiewicz A, Forró L, Kiwi J, Pulgarin C (2009) Appl Catal B 88:398
52. Wei F, Ni L, Cui P (2008) J Hazard Mater 156:135
53. Wang X, Lim T-T (2010) Appl Catal B 100:355
54. Diwald O, Thompson TL, Zubkov T, Walck SD, Yates JT (2004) J Phys Chem B 108:6004
55. Sun H, Bai Y, Cheng Y, Jin W, Xu N (2006) Ind Eng Chem Res 45:4971
56. Lee HU, Lee Y-C, Lee SC, Park SY, Son B, Lee JW, Lim C-H, Choi C-J, Choi M-H, Lee SY, Oh Y-K, Lee J (2014) Chem Eng J 254:268
57. Fan D, Weirong Z, Zhongbiao W (2008) Nanotechnology 19:365607
58. Chen X, Burda C (2004) J Phys Chem B 108:15446
59. Sathish M, Viswanathan B, Viswanath RP, Gopinath CS (2005) Chem Mater 17:6349
60. György E, Pérez del Pino A, Serra P, Morenza JL (2003) Surf Coat Technol 173:265
61. Park J-Y, Lee C, Jung K-W, Jung D (2009) Bull Korean Chem Soc 30:402
62. Prasai B, Cai B, Underwood MK, Lewis JP, Drabold DA (2012) J Mater Sci 47:7515
63. Kramer B, Maschke K, Thomas P (1971) Phys Status Solidi B 48:635
64. Banerjee S, Pillai SC, Falaras P, O'Shea KE, Byrne JA, Dionysiou DD (2014) J Phys Chem Lett 5:2543
65. Li J-G, Tang C, Li D, Haneda H, Ishigaki T (2004) J Am Ceram Soc 87:1358
66. Perego C, Wang Y-H, Durupthy O, Cassaignon S, Revel R, Jolivet J-P (2012) ACS Appl Mater Interfaces 4:752
67. Sato T, Aita Y, Komatsu M, Yin S (2006) J Mater Sci 41:1433
68. García-Valenzuela JA (2017) Comments Inorg Chem 37:99
69. Li Z, Cong S, Xu Y (2014) ACS Catal 4:3273
70. Ohtani B (2014) Electrochemistry 82:414
71. Ohtani B (2014) Phys Chem Chem Phys 16:1788
72. Henderson MA (2011) Surf Sci Rep 66:185
73. Liu K-I, Su C-Y, Perng T-P (2015) RSC Adv 5:88367
74. Zhao Y, Huang X, Tan X, Yu T, Li X, Yang L, Wang S (2016) Appl Surf Sci 365:209
75. Rtimi S, Pulgarin C, Sanjines R, Kiwi J (2015) Appl Catal B 162:236
76. Krumova K, Cosa G (2016) In: Nonell S, Flors C (eds) Singlet oxygen: applications in biosciences and nanosciences, vol 1. The Royal Society of Chemistry, Cambridge, ch. 1
77. Houas A, Lachheb H, Ksibi M, Elaloui E, Guillard C, Herrmann JM (2001) Appl Catal B 31:145
78. Tomić N, Grujić-Brojčin M, Finčur N, Abramović B, Simović B, Krstić J, Matović B, Šćepanović M (2015) Mater Chem Phys 163:518
79. Luo B, Li Z, Xu Y (2015) RSC Adv 5:105999
80. Luís AM, Neves MC, Mendonça MH, Monteiro OC (2011) Mater Chem Phys 125:20
81. Yang W, Wen Y, Zeng D, Wang Q, Chen R, Wang W, Shan B (2014) J Mater Chem A 2:20770
82. Scanlon DO, Dunnill CW, Buckeridge J, Shevlin SA, Logsdail AJ, Woodley SM, Catlow CR, Powell MJ, Palgrave RG, Parkin IP, Watson GW, Keal TW, Sherwood P, Walsh A, Sokol AA (2013) Nat Mater 12:798
83. Cataldo S, Sartorio C, Giannazzo F, Scandurra A, Pignataro B (2014) Nanoscale 6:3566